Development of PAN/ZrO_2 Nanocomposite Material with Perovskite $CsPbBr_3$ Filler As a CO_2 Adsorbent

Akhdan Fadhil Muhammad[a*], Azzah Dyah Pramata[b]

[a]*Master Degree Programs in Material and Metallurgical Engineering, Institut Teknologi Sepuluh Nopember, Surabaya 60111, Indonesia*
[b]*Department of Material and Metallurgical Engineering, Institut Teknologi Sepuluh Nopember, Surabaya 60111, Indonesia*

**Corresponding author's email: azzah@its.ac.id*

Received: 10 April 2025 **Revised: 23 June 2025** **Accepted: 30 July 2025**

Available Online: 30 August 2025

ABSTRACT

The increasing need for effective CO_2 capture has driven interest in nanofiber-based materials due to their high surface area and tunable structure. This study reports the fabrication and characterization of PAN-based nanofibers incorporated with $CsPbBr_3$ perovskite and ZrO_2 nanoparticles via electrospinning, aiming to enhance CO_2 adsorption performance. Morphological and structural analyses confirmed that $CsPbBr_3$ improves adsorption sites, while ZrO_2 enhances thermal and mechanical stability. Kinetic evaluations using Pseudo-First-Order (PFO), Pseudo-Second-Order (PSO), and Intraparticle Diffusion models showed that the PFO model provided the best fit, with AFM–5 achieving the highest adsorption capacity (376.82 mg/g). The adsorption mechanism was identified as predominantly physical (physisorption), supported by significant intraparticle diffusion, particularly in ZrO_2-containing samples. FTIR and BET analysis verified improved structural integrity and functional group interactions. These findings suggest that PAN/ZrO_2/$CsPbBr_3$ nanofibers are promising candidates for CO_2 capture in direct air capture and industrial gas separation applications.

Keywords: CO_2 adsorption, PAN nanofiber, $CsPbBr_3$ perovskite, ZrO_2, physisorption, kinetic modeling, electrospinning

1. Introduction

The increasing concentration of CO_2 in the atmosphere has led to widespread concerns due to its direct impact on climate change, global warming, and environmental degradation. Industrial activities, fossil fuel combustion, and deforestation have significantly contributed to elevated CO_2 levels, emphasizing the need for advanced carbon capture technologies. Traditional CO_2 capture techniques, such as amine scrubbing, have been widely employed, but these methods pose challenges including high energy consumption, corrosion, and limited long-term stability (Shah et al., 2021). Consequently, alternative materials with enhanced adsorption capabilities, improved stability, and cost-effectiveness have been the focus of recent research (Patel et al., 2017).

Nanofiber-based adsorbents have gained increasing attention for CO_2 capture due to their high surface area, tunable porosity, and excellent chemical functionality. Among the polymeric materials used, polyacrylonitrile (PAN) nanofiber**s** stand out due to their high nitrogen content, which provides active adsorption sites for CO_2 (Ma et al., 2023). PAN contains nitrile (-C≡N) functional groups that facilitate CO_2 adsorption through physisorption and chemisorption mechanisms (Tourzani et al., 2023). The ability of PAN nanofibers to capture CO_2 is primarily due to the presence of nitrile (-C≡N) groups, which enhance CO_2 solubility and selectivity (Beltzung et al., 2018). The high polarity of nitrile groups allows strong interactions with CO_2 molecules through dipole-quadrupole interactions. PAN nanofibers act as both gas barriers and active CO_2 adsorption sites, selectively retaining CO_2 molecules while allowing nitrogen (N_2) to pass through (Kwon et al., 2022). The adsorption process occurs in two stages: physisorption and chemisorption. Physisorption is a reversible process, where CO_2 molecules weakly interact with nitrile groups through van der Waals forces and electrostatic interactions, enabling easy desorption and regeneration (Darmayanti et al., 2024; Moore et al., 2018; Zaker et al., 2023). Chemisorption, on the other hand, involves stronger interactions, forming covalent bonds between CO_2 and nitrile functional groups. This occurs through nucleophilic attack, leading to the formation of carbamate (-NHCOO-) complexes, which improve long-term CO_2 retention (Quan et al., 2023). Studies have shown that PAN nanofibers exhibit CO_2 adsorption capacities of 3.95 mmol/g at 1 bar and 25 °C**,** making them highly competitive for carbon capture applications (Ma et al., 2023). The porous structure of electrospun PAN nanofibers further enhances adsorption efficiency by increasing available surface area and diffusion pathways (Shaki, 2023).

Polyacrylonitrile (PAN) is used as the polymer matrix due to its high carbon yield and excellent mechanical properties. PAN is well known for its ability to form nanofibers through electrospinning, offering a high surface area that facilitates effective gas adsorption. Electrospinning is a versatile and efficient method for fabricating nanofibers with controlled morphology and composition. It allows for precise tuning of fiber diameter and porosity, which are critical for adsorption applications. The technique involves applying a high-voltage electric field to a polymer solution, generating fine nanofibers as the solution is ejected from a syringe toward a collector. This process enables the production of nanofibers with a high surface-to-volume ratio, improving interaction sites for CO2 adsorption. Additionally, electrospinning allows for the incorporation of various functional materials, such as perovskites, into the polymer matrix, ensuring uniform dispersion and enhanced material properties (Ahmadi Bonakdar and Rodrigue, 2024; Avossa et al., 2022). Several key parameters influence the success of the electrospinning process, including solution parameters, process parameters, and environmental conditions. The solution parameters include polymer concentration, viscosity, conductivity, and solvent volatility, all of which determine fiber formation and morphology. A well-balanced polymer concentration is essential to avoid bead formation or excessively thick fibers. The process parameters encompass applied voltage, flow rate, needle-to-collector distance, and collector type. These factors significantly impact fiber diameter, uniformity, and alignment. For instance, increasing the applied voltage enhances fiber stretching, resulting in finer fibers, while an optimized flow rate ensures a steady fiber deposition without excessive bead formation. Environmental conditions, such as humidity and temperature, also play a crucial role in electrospinning. High humidity can lead to the formation of porous fibers due to rapid solvent evaporation, whereas temperature variations affect solvent evaporation rates and fiber solidification (Bakar et al., 2018; Barua and Saha, 2018; Beknalkar et al., 2021; Fajariah et al., 2023; Liu et al., 2019).

Zirconium dioxide (ZrO_2) is a ceramic material known for its excellent thermal stability, high mechanical strength, and chemical inertness. ZrO_2 exists in three primary crystal structures. Monoclinic ZrO_2 (m-ZrO_2) is stable at room temperature up to 1170 °C**,** but prone to phase transformation under high temperatures (Song et al., 2023). Tetragonal ZrO_2 (t-ZrO_2) is stable between 1170 °C and 2370 °C, offering improved mechanical strength due to its stress-induced phase transformation. Cubic ZrO_2 (c-ZrO_2) is stable above 2370 °C, exhibiting high ionic conductivity and superior thermal resistance (Zhou et al., 2021). The tetragonal phase is particularly effective for CO_2 adsorption due to the presence of coordinatively unsaturated sites (CUS), which function as Lewis acid and Brønsted base sites, facilitating stronger CO_2 binding (Köck et al., 2017). Studies indicate that t-ZrO_2 outperforms the monoclinic phase in terms of CO_2 adsorption capacity, carbonate stability, and reversibility (Zhou et al., 2021).

Each material used in this study possesses unique properties that contribute to the overall performance of the nanofiber composite**.** $CsPbBr_3$ (Cesium Lead Bromide Perovskite) has a band gap of 2.3 eV, high charge carrier mobility, and defect tolerance, making it suitable for optoelectronic applications. However, it is degradation-prone under high temperature and humidity (Pan et al., 2022). PAN (Polyacrylonitrile) Nanofibers exhibit high thermal resistance, a nitrogen-rich composition with nitrile (-C≡N)

functional groups for CO_2 adsorption, and an electrospun porous structure that enhances permeability and gas selectivity, achieving an adsorption capacity of 3.95 mmol/g (Ma et al., 2023). ZrO_2 (Zirconium Dioxide) provides thermal stability up to 2900 °C**,** high mechanical strength, and Lewis acid sites that enhance CO_2 adsorption, while also improving the structural integrity of perovskite-polymer composites (Zhou et al., 2021).

The incorporation of ZrO_2 into $CsPbBr_3$/PAN nanofibers is expected to address key limitations associated with both polymer and perovskite-based adsorbents. By introducing ceramic nanoparticles, the composite nanofibers can benefit from enhanced mechanical robustness, increased thermal stability, and improved CO_2 adsorption efficiency (Zhou et al., 2021)). The interaction between ZrO_2 and PAN facilitates better dispersion of $CsPbBr_3$ within the polymer matrix, preventing aggregation and ensuring a more uniform distribution of active sites (Shi et al., 2024). This study aims to synthesize and characterize $CsPbBr_3$/PAN/ZrO_2 nanofibers to evaluate their structural integrity and CO_2 adsorption capabilities. The nanofibers will be fabricated using electrospinning (Bonakdar et al., 2023), followed by thermal and structural characterizations utilizing Scanning Electron Microscopy (SEM), Energy Dispersive X-ray Spectroscopy (EDX), Fourier Transform Infrared (FTIR) Spectroscopy, and CO_2 Adsorption as the performance test. This research is still on progress. The ultimate goal of this research is to establish the feasibility of $CsPbBr_3$/PAN/ZrO_2 composite nanofibers as a novel material for high-performance CO_2 capture applications.

2. Material And Methods

2.1 Material

Lead(II) Bromide ($PbBr_2$. 98%), Cesium Bromide (CsBr, 99% trace metal basis), Oleic Acid Technical Grade 90%, Octylamine, Hexane (n-Hexane for analysis), Distilled Water (water for analysis), N, N-Dimethylformamide (DMF, 99%), Acetone, Toluene, Polyacrylonitrile (PAN, 99%), Zirconium(IV) Oxide (Nanopowder, 100 nm particle size (TEM)) were purchased from Sigma Aldrich. All materials were commercially available and used without any further purification.

2.2 Experimental Procedure

2.2.1 Preparation of $CsPbBr_3$ Perovskite

Cesium bromide (CsBr) with a concentration of 0.3 mmol was dissolved in 0.3 mL of distilled water in a beaker under continuous stirring at 700 rpm using a magnetic bar while being heated to 60°C until fully dissolved. Simultaneously, 0.3 mmol of lead(II) bromide ($PbBr_2$) was dissolved in 0.5 mL of dimethylformamide (DMF) under identical stirring and heating conditions. During this process, a separate solution consisting of 10 mL of n-hexane, 2 mL of oleic acid, and 0.25 mL of octylamine was prepared using a micropipette. This solution was then added to the previously prepared CsBr and $PbBr_2$ solutions. The resulting mixture was stirred at 50°C for 3 minutes until fully dissolved, leading to the formation of $CsPbBr_3$.The $CsPbBr_3$ solution was transferred into a centrifuge bottle and centrifuged at 7000 rpm for 10 minutes. After centrifugation, the precipitate (yield) and supernatant were separated. The supernatant was discarded, and the precipitate was washed using 0.2 mL of acetone and 0.8 mL of toluene at a 1:4 ratio. The variation of the samples are available at sample code.

2.2.2 Preparation of $CsPbBr_3$/PAN/ZrO_2

Dissolve 0.1 g of ZrO_2 in 13 mL of DMF solvent using an ultrasonic bath at 70°C for 1 hour to ensure proper dispersion. Once homogenized, transfer the ZrO_2 solution to a hotplate and add 0.4 g of PAN while stirring at 500 rpm and 25°C for 12 hours. During the stirring process, introduce 1 mL of $CsPbBr_3$ **s**olution into the PAN/ZrO_2 mixture and continue stirring for 4 hours at the same temperature and speed. After stirring, load the $CsPbBr_3$/PAN/ZrO_2 solution into a syringe for electrospinning. The electrospinning process is performed at a flow rate of 1 mL/h**, a** voltage of 14-15 kV, and **a** collector distance of 18 - 20 cm. Once the electrospinning process is complete, $CsPbBr_3$/PAN/ZrO_2 nanofibers are collected and stored in a sealed container to prevent material degradation. Additionally, 1 mL of washed $CsPbBr_3$ solution is added dropwise into the PAN/ZrO_2 solution while stirring using micropipette and the process continues for another 4 hours to ensure proper integration.

2.2.3 Measurement procedure of CO_2 adsorption performance potential

The specimen was prepared and placed into a beaker glass. A 0.05M KOH electrolyte solution was added to the beaker glass. The solution was then connected to a potentiostat using a three-electrode system. The beaker glass was exposed to UV light to initiate the reaction. The reaction results were recorded and displayed on an electronic device equipped with the Cs Studio application. After the experiment, the chamber was cleaned.

2.3 Characterization

Fourier transform infrared spectroscopy (FTIR; Shimadzu) was employed to analyze the characteristics of functional groups. The crystal structure was analyzed using an X-ray diffractometer (XRD; PANalytical X'pert PRO). The morphology was characterized using a scanning electron microscope (SEM; JSM-IT510+Oxford. JEOL), complemented by X-ray energy – dispersive

spectroscopy – mapping (EDS) to measure the elemental content. The specific surface area and pore size were analyzed using fully automatic specific surface area and porosity analyzer (BET; EASY V). identification of the thermal properties of the product obtained, thermal stability of the product, identification of the composition and characterization of phase changes or degradation of the material at a certain temperature were analyzed using different thermal analysis and thermogravimetric analysis (DTA/TGA; Shimadzu). For the mechanical characteristics of the product produced, specifically the product's ability to withstand tensile forces before being damaged, it was carried out using tensile test (TVO 1000N500S Sauter/Compression). To determine the CO_2 adsorption capacity, material interaction with CO_2 gas, as well as the adsorption-desorption stability under certain conditions on nanofibers was carried out using CO_2 adsorption analysis.

2.4 Sample Code

Table 1. Material composition of PAN, DA – 2, and AFM – 5

PAN : ZrO2 : CsPbBr3 Ratio (wt%)	Sample Code
100% - 0 - 0	PAN
28.57% - 0 - 71.43%	DA-2
11.75% - 0.15% - 88.10%	AFM-5

All of the variations are coded. So it will be easy to know the differences between each other. The variations are done using the wt% comparison. The additional 0.15% ZrO_2 was synthesized for AFM – 5. If the mass when adding ZrO_2 is used too much, it will produce a product with a high viscosity level. This can make nanofiber fabrication difficult to do. Therefore the mass of ZrO_2 used is 0.01 grams or 0.15 wt%.

3. Results and Discussions

3.1 *SEM – EDX Analysis Result*

The SEM-EDX analysis was conducted to evaluate both the morphological and elemental composition characteristics of $CsPbBr_3$/PAN nanofibers synthesized through electrospinning. Scanning Electron Microscopy (SEM) provides detailed imaging of the nanofiber structure, revealing its uniformity, fiber diameter, and overall surface morphology. Meanwhile, Energy Dispersive X-ray Spectroscopy (EDX) was utilized to confirm the elemental distribution and compositional homogeneity of $CsPbBr_3$ within the PAN matrix. This dual characterization approach allows for a comprehensive understanding of the material's structural integrity and elemental dispersion, which are crucial factors in optimizing its performance for CO2 adsorption applications.

The morphological analysis of PAN nanofibers using SEM revealed in Fig. 1, that the fibers were uniform, continuous, and free from significant bead formation. The diameter of the PAN nanofibers was relatively consistent, confirming that the electrospinning parameters were well-optimized. The porous nature of the fibers suggests their suitability for CO_2 adsorption applications. Elemental analysis using EDX confirmed the presence of carbon (C), nitrogen (N), and oxygen (O), which are characteristic components of PAN. Small traces of aluminum (Al) were also detected, likely originating from the aluminum foil used as the electrospinning collector. The homogeneous distribution of PAN components ensures the formation of a stable nanofiber network, facilitating high porosity essential for gas adsorption. The SEM analysis of DA – 2 nanofibers showed in Fig. 2, that the presence of CsPbBr3 altered the fiber morphology, resulting in slightly larger fiber diameters compared to pure PAN. The interconnected fibrous network was still maintained, though minor irregularities in fiber structure were observed. EDX mapping confirmed the presence of carbon (C), nitrogen (N), oxygen (O), bromine (Br), lead (Pb), and cesium (Cs). The distribution of CsPbBr3 within the nanofibers was generally uniform, though slight agglomeration was noted in certain areas, which may affect the adsorption efficiency. The increase in CsPbBr3 concentration enhances the functional properties of the nanofiber, improving its potential for CO2 capture while slightly affecting structural uniformity. In AFM – 5 that shown in Fig. 3, the higher proportion of CsPbBr3 resulted in further changes to fiber morphology. The fiber diameter was slightly larger than DA – 2, and more pronounced fiber clustering was observed. This may be due to increased perovskite loading, affecting the viscosity of the electrospinning solution. EDX analysis confirmed a higher intensity of Br, Pb, and Cs signals compared to DA – 2, indicating a greater CsPbBr3 content. The distribution was still relatively uniform but with more noticeable regions of aggregation, suggesting that further optimization in precursor mixing could enhance homogeneity. The increased presence of CsPbBr3 in AFM – 5 provides greater adsorption potential but also poses challenges in maintaining fiber stability due to increased material clustering. As shown in Fig. 3, the incorporation of ZrO_2 demonstrates a clear advantage with less beads than PAN and DA – 2. In comparison to DA – 2 in Fig. 2, the number of formed beads is significantly reduced. This suggests that the addition of ZrO_2 to the $CsPbBr_3$

nanofiber composite effectively minimizes bead formation, thereby potentially enhancing the nanofiber's CO_2 adsorption performance

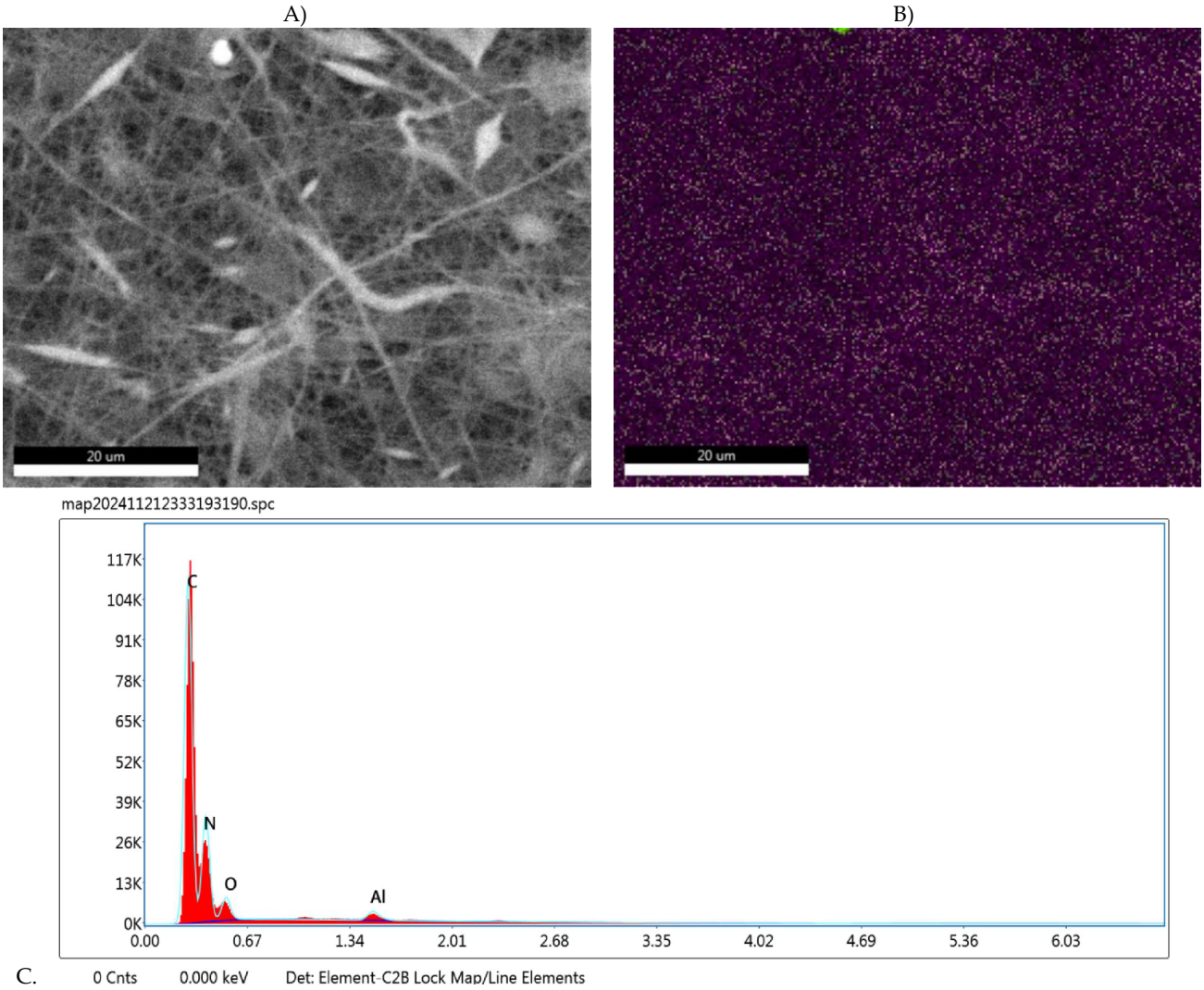

Figure 1. The result of SEM-EDX Mapping of PAN, with A.) morphology of PAN Nanofiber; B) SEM-Mapping of PAN elemental; and C.) the measure elemental content of PAN

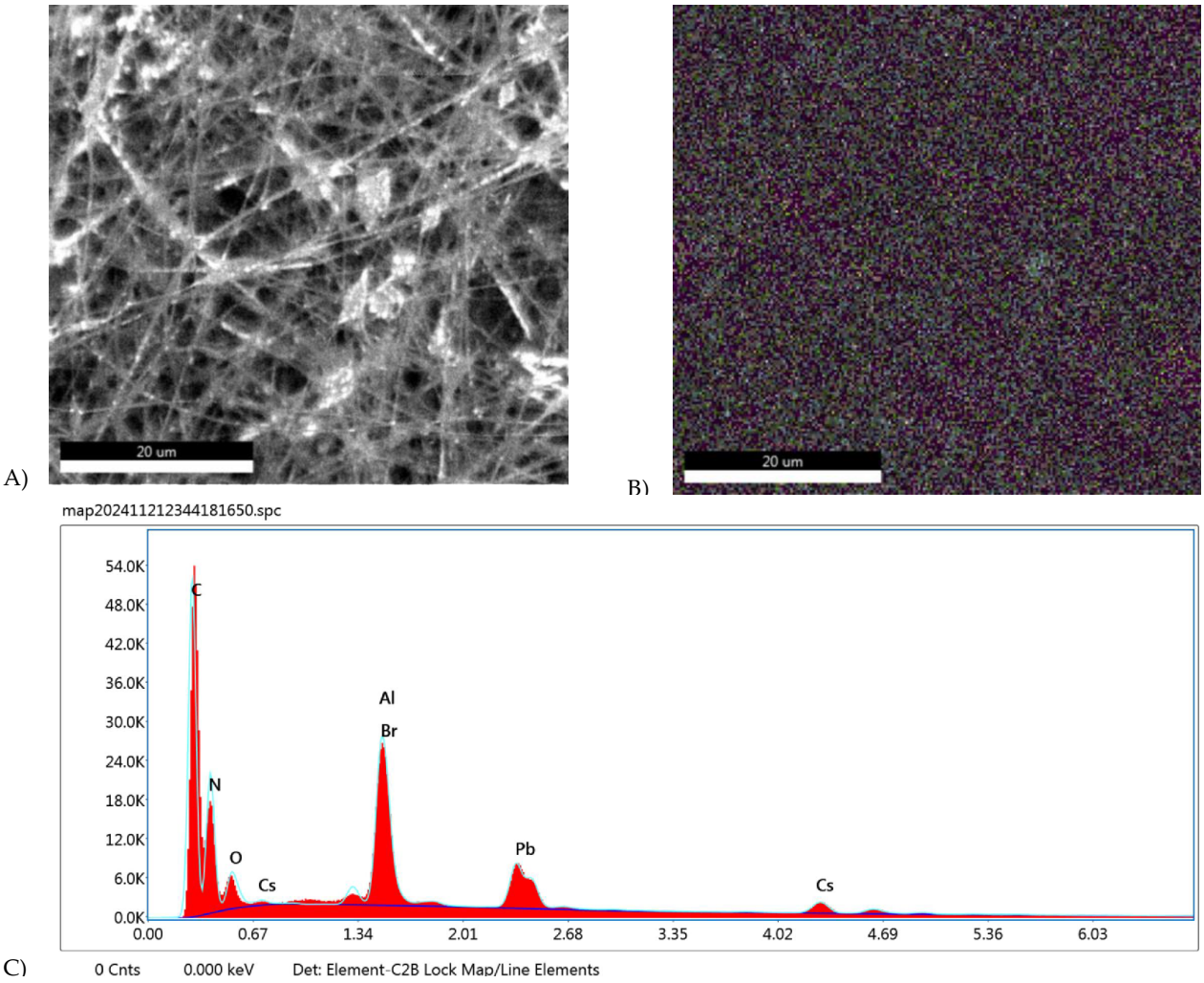

Figure 2. The result of SEM-EDX Mapping of DA – 2, with A.) morphology of DA – 2; B.) SEM-Mapping of DA – 2 elemental; and C.) The measure elemental content of DA – 2

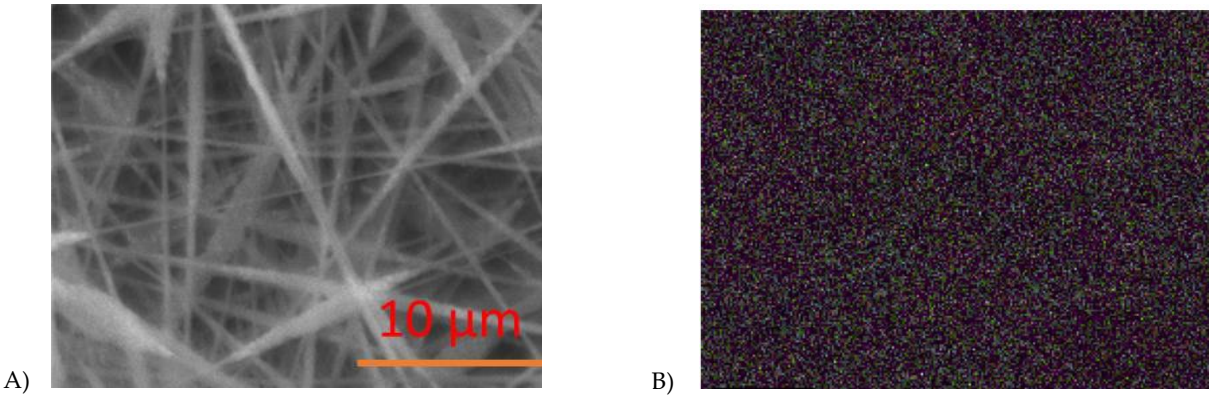

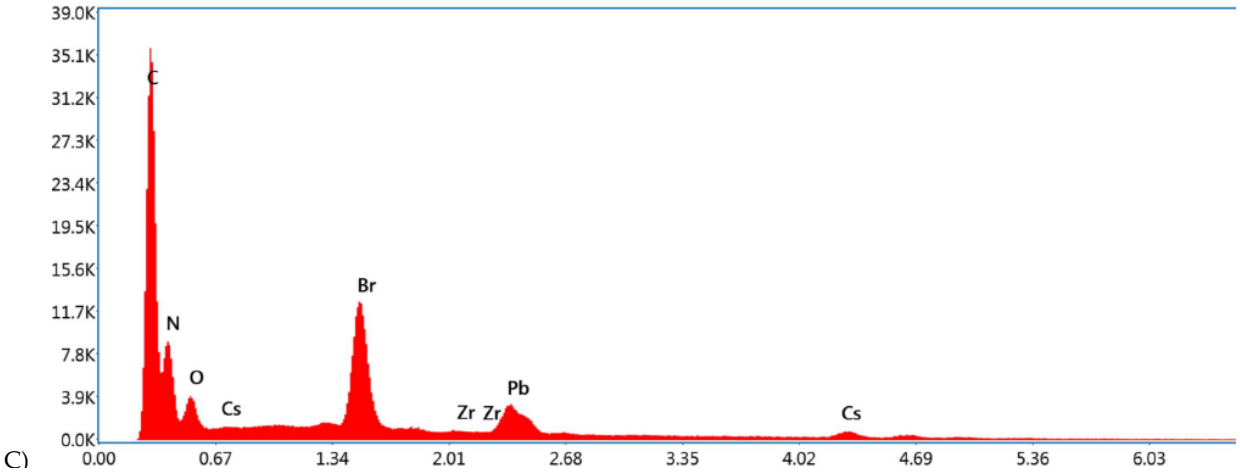

C)

Figure 3. The result of SEM-EDX Mapping of AFM -- 5, with A.) morphology of AFM – 5; B.) SEM-Mapping of AFM – 5 elemental; and C.) The measure elemental content of AFM – 5.

Previous research has been conducted by Lusiola, *et al*. 2023 using the Zr-nanoparticles system and Zirconium(IV) Carbonate hydroxide system as the main material and electrospinning as the method for nanofiber fabrication. In this study, modifications were made by incorporating zirconia into the nanofiber structure, which resulted in structural imperfections such as bead formation and uneven fiber distribution. This issue is common in electrospun fibers when the polymer solution has imbalanced properties such as viscosity, conductivity, and surface tension, leading to unstable fiber formation. The presence of beads in electrospun nanofibers is often undesirable, as it can negatively affect the surface area, mechanical properties, and overall performance of the material in various applications, including adsorption and catalysis.

In Fig. 4, the SEM image presents the morphology of the nanofiber before the introduction of zirconia. The fibers appear highly irregular, with noticeable bead formation along the fiber structure, suggesting that the electrospinning process was not fully optimized. Bead formation typically occurs when the polymer jet during electrospinning fails to maintain a continuous stretching process, resulting in the partial coalescence of polymer droplets rather than the formation of smooth, elongated fibers. This issue could be linked to inadequate polymer concentration, improper solvent selection, or inconsistent electric field conditions during electrospinning. The presence of beads indicates that the fiber network may have lower porosity and surface area, which can reduce its efficiency in applications requiring high interaction with external molecules, such as gas adsorption or catalysis. Additionally, the fiber diameters in this figure appear widely varied, further reinforcing the notion that the electrospinning process was unstable. Without zirconia, the fibers might lack structural reinforcement, making them more prone to deformation or poor mechanical integrity.

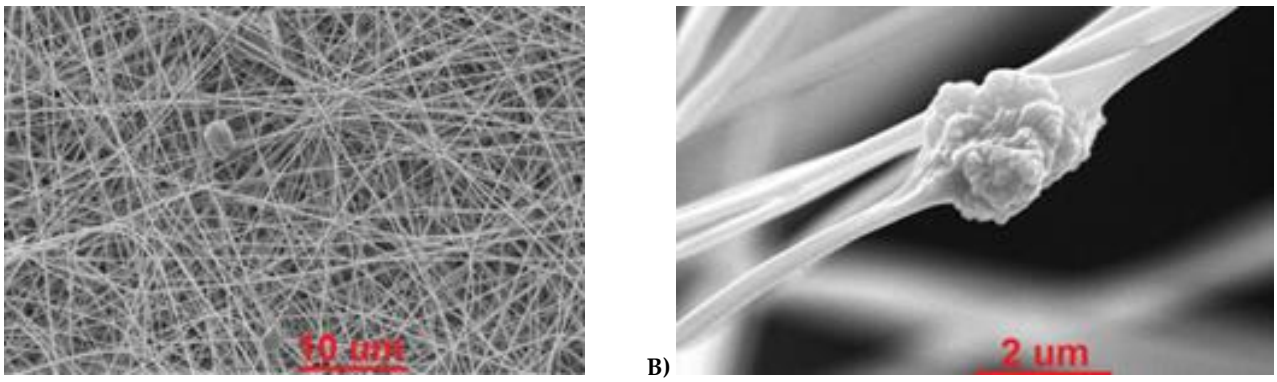

A) B)

Figure 4. Electrospun fibers produced using electrospinning solution that did not fully sediment and before calcination heat treatment at 1000 ^{o}C , -based system showing particles; A.) between and B.) in fibers.(Lusiola et al., 2023)

A significant transformation is observed in Fig 5, which showcases the nanofiber after being modified with zirconia. The morphology of the fibers appears much more uniform, with a noticeable reduction in bead formation. This improvement suggests that the addition of zirconia has played a crucial role in stabilizing the electrospinning process. One possible explanation is that zirconia particles influence the viscosity and conductivity of the polymer solution, enabling a more stable and continuous jet formation. When properly incorporated, zirconia can enhance the charge distribution within the electrospinning solution,

reducing the likelihood of bead formation and promoting smoother fiber elongation. As a result, the fibers in Figure 9 display a more homogeneous structure with relatively consistent diameters, indicating a successful optimization of the electrospinning parameters.

A) 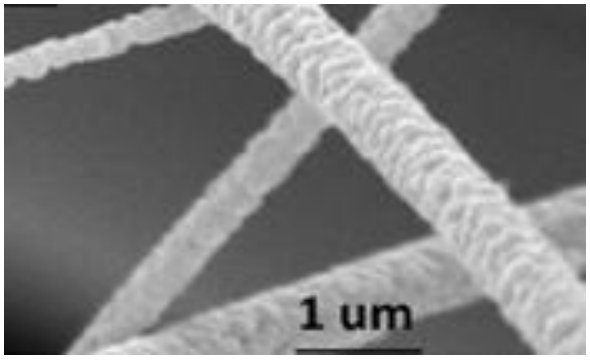

B) 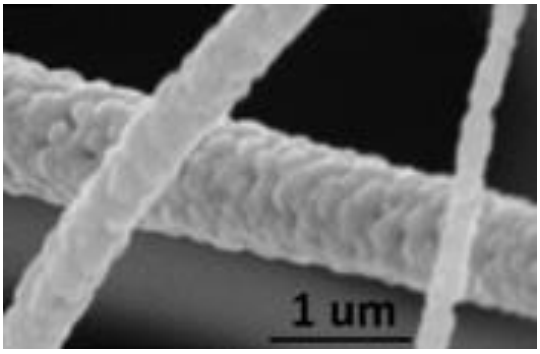

Figure 5. Calcined fibers from the; A.) zirconia nanoparticle system; B.) zirconium (IV)-carbonate system at 1000 °C (Lusiola et al., 2023)

Another significant change in Fig 5 is the surface texture of the fibers, which appears notably rougher compared to the smooth fibers in Fig 4. This increased roughness suggests that zirconia particles have either been embedded within the polymer matrix or have coated the fiber surface during the electrospinning process. This surface modification is critical for various functional applications, as rougher surfaces often lead to increased surface area and enhanced interaction sites, which are beneficial in adsorption-based applications, catalytic reactions, or even biomedical uses such as drug delivery. Furthermore, the enhanced roughness may indicate a change in the overall mechanical properties of the nanofibers, potentially making them more durable or resistant to structural collapse under stress. Beyond morphological improvements, the reduction in bead formation and the incorporation of zirconia may also contribute to enhanced thermal and chemical stability. Zirconia is known for its high thermal resistance and excellent chemical stability, which means that nanofibers embedded with zirconia could exhibit improved durability under extreme conditions. In many adsorption and catalytic applications, nanofibers must withstand exposure to high temperatures, moisture, or reactive gases. The improved structural integrity observed in Fig 5 suggests that zirconia incorporation might help the nanofiber maintain its performance over extended periods of use.

In conclusion, Fig 5 represents the nanofiber before modification, characterized by a highly irregular morphology, significant bead formation, and inconsistent fiber distribution, all of which suggest an unstable electrospinning process. In contrast, Fig 5 illustrates a more optimized nanofiber structure after zirconia incorporation, with a significant reduction in bead formation, more uniform fiber diameters, and a rougher surface texture, which suggests successful material integration and potential improvements in functional properties. The incorporation of zirconia not only improves the electrospinning process but also enhances the nanofiber's overall structural and potential functional performance.

3.2 *XRD Analysis Result*

Based on Fig **6** the calcination process at 1000°C significantly influences the crystalline structure and phase composition of the material. At this high temperature, the transformation from an amorphous or metastable phase to a more thermodynamically stable crystalline phase is evident. The XRD pattern likely reveals well-defined diffraction peaks, indicating an increase in crystallinity due to the enhanced atomic ordering. The peak positions and intensities provide insight into the symmetry and unit cell parameters of the formed phase.

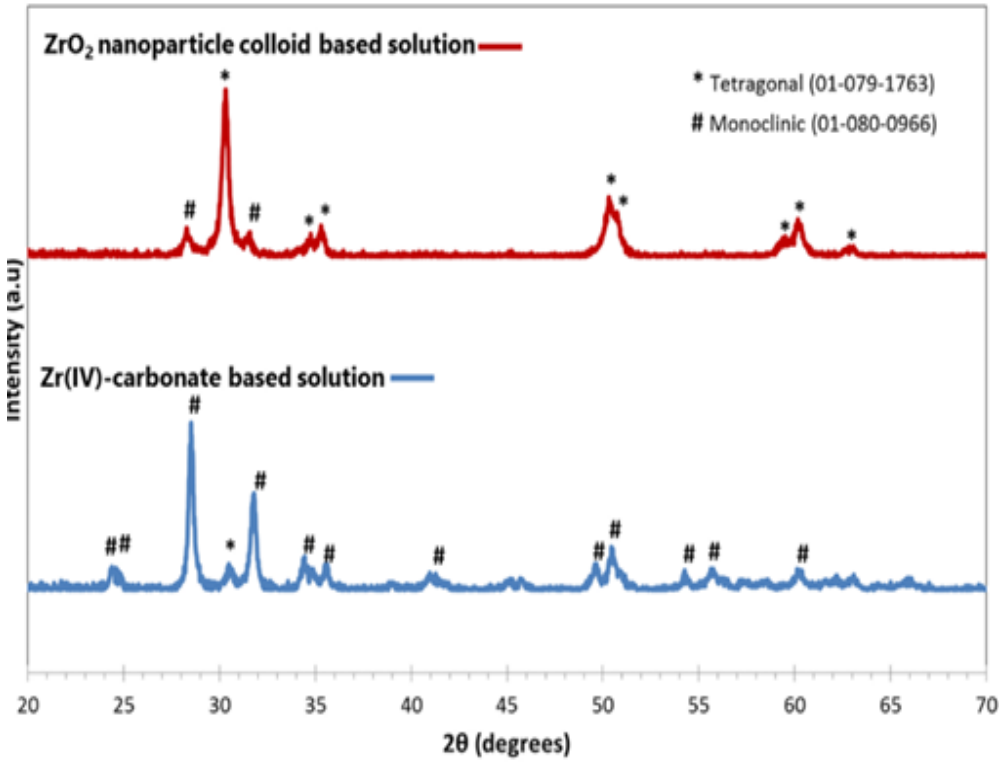

Figure 6. X-ray diffraction patterns of calcined ZrO 2 nanofibers from the zirconia nanoparticle system and zirconium carbonate system, showing different crystal line phases. (Lusiola et al., 2023)

For zirconia (ZrO_2) materials subjected to 1000°C calcination, the predominant phase transition is expected to be from a tetragonal (t-ZrO_2) to a monoclinic (m-ZrO_2) structure. This transformation is characterized by the appearance of distinct peaks in the XRD pattern. The tetragonal phase typically exhibits diffraction peaks around 30.2°, 50.3°, and 60.1°, while the monoclinic phase shows characteristic peaks at approximately 28.2°, 31.5°, and 34.3°. If the XRD results indicate a dominance of monoclinic peaks, it suggests that the high calcination temperature promotes the complete phase transformation, which may affect material properties such as surface area, porosity, and mechanical stability.

Additionally, the peak broadening or sharpening provides further information regarding crystallite size and strain. Sharper peaks imply increased crystallite growth and reduced lattice strain, confirming that prolonged exposure to 1000°C leads to a highly ordered structure. If secondary phases or shifts in peak positions are observed, they may indicate the presence of dopants or lattice distortions. Overall, the XRD results at 1000°C suggest a structural reconfiguration towards a stable equilibrium state, impacting the symmetry and physical properties of the nanofibrous material. (Lusiola et al., 2023).

3.4 *FTIR Analysis Result*

Fourier-transform infrared (FTIR) spectroscopy was employed to investigate the chemical structure and interactions within the composite nanofibers. The FTIR spectrum of pure polyacrylonitrile (PAN) exhibits a distinct and sharp absorption peak centered at approximately 2243 cm^{-1}, which is characteristic of the stretching vibration of the nitrile group (–C≡N). This observation confirms the presence of intact PAN chains within the nanofiber matrix. Additional absorption bands located around 2930 cm^{-1} and in the range of 1450–1350 cm^{-1} correspond to the stretching and bending vibrations of CH_2 groups, respectively, which are typical vibrational features of PAN.

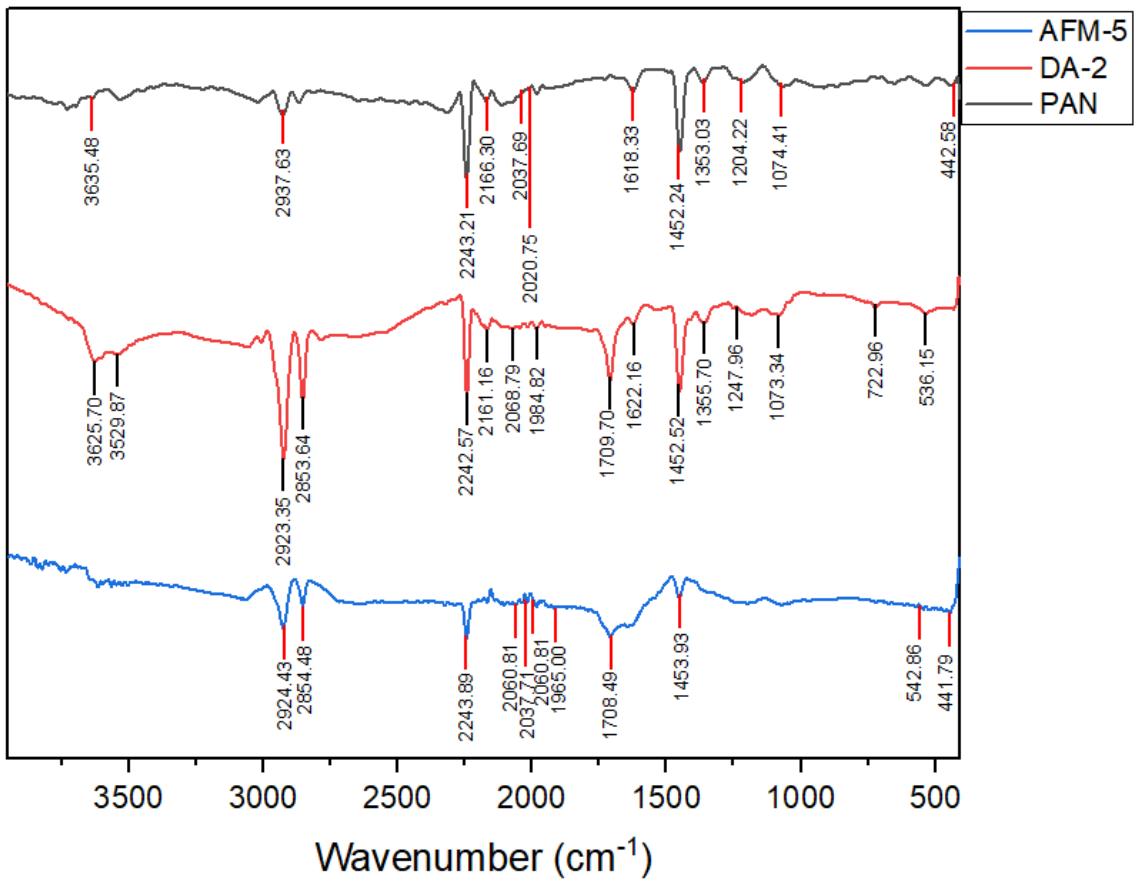

Figure 7. The IR Spectra Of PAN. DA – 2, and AFM – 5

Upon incorporation of cesium lead bromide ($CsPbBr_3$) into the PAN matrix to form the DA – 2 sample, the FTIR spectrum retains the nitrile peak at 2243 cm^{-1}, indicating that the PAN structure remains chemically stable and unaltered. Notably, new absorption features emerge in the region of 540–570 cm^{-1}, which are attributed to the Pb–Br stretching vibrations. These peaks serve as vibrational fingerprints of the perovskite phase, thereby confirming the successful inclusion of $CsPbBr_3$ into the composite. The absence of significant shifts in the main PAN absorption bands suggests that the interaction between PAN and $CsPbBr_3$ is predominantly physical rather than chemical, implying that the two components coexist in a mixed state without strong interfacial bonding.

Tabel 2. The FTIR Interpretation of PAN, DA – 2, and AFM – 5

Wavenumber (cm^{-1})			Interpretation	References
PAN	**DA-2**	**AFM-5**		
3635.48	3625.70 3529.87	-	Vibration O-H Bond, Stretching of N-H	(Guo et al., 2025; Mahmood and Jawad, 2019)
2937.63	2923.35 2853.64	2924.43 2854,48	Stretching C-H band in CH_2, C-H tensile vibrations	(Hongyu Chen et al., 2021; Mahmood and Jawad, 2019)
2243.21 **2166.30** **2037.69** **2020.75**	2242.57 2161.16 2068,79 1984.82	2243.89 2060,81 2037.71 2019.82 1965.00	C≡N stretching of acrylonitrile unit	(Mahmood and Jawad, 2019)
1618.33	1709.70 1622.16	1709.49	C=O (Carbonyl) and C=C Vibartions, NH_2 bending vibration, C=O stretching vibration. O-H stretching and bending Vibration.	(Akhil et al., 2021; Mahmood and Jawad, 2019)
1452.24	1452.52	1453.93	C-H tensile Vibration in CH_2 group, $–CH_2$ bending vibration from the ligands of oleic acid and octylamine	(Mahmood and Jawad, 2019; Wang et al., 2024)
1353.03	1355.70	-	C-H stretching in aliphatic group, COO^- and CH_3 groups stretching	(Haitao Chen et al., 2021; Mahmood and Jawad, 2019)
1204.22	1247.96	-	C-O Vibration in acetate group	(Mahmood and Jawad, 2019)
1074.41	1073.34	-	C-O groups	(Mahmood and Jawad, 2019)
442.58	722.96 536.15	542.86 441.79	C-H stretching band, C-Br stretching vibrations, tetragonal Zr-O vibration	(Guo et al., 2025; Mahmood and Jawad, 2019)

In contrast, the FTIR spectrum of the AFM-5 sample, which includes zirconium dioxide (ZrO_2) in addition to $CsPbBr_3$ and PAN, reveals further spectral modifications. Besides the characteristic absorption peaks of PAN and the Pb–Br vibrations, broad bands appear below 700 cm^{-1}, which can be assigned to Zr–O stretching modes. The appearance of these features confirms the successful incorporation of ZrO_2 into the composite structure. More importantly, slight shifts in the positions of the nitrile and Pb–Br peaks are observed, suggesting the presence of chemical interactions or interfacial bonding between the components. These spectral changes imply a higher degree of structural integration among PAN, $CsPbBr_3$, and ZrO_2 in the AFM-5 sample, potentially leading to the formation of a more unified hybrid nanostructure.

In summary, the FTIR analysis verifies the presence and structural integrity of each constituent material within the composite nanofibers. The increasing spectral complexity and observed peak shifts in AFM-5 indicate enhanced chemical interactions, which may contribute to improved structural stability and synergistic functionality in the final hybrid nanofiber system.

3.5 *CO_2 Adsorption Analysis Result*

CO_2 adsorption testing was conducted to determine the CO_2 adsorption capacity, material interaction with CO_2 gas, and adsorption stability under certain conditions on PAN, AFM-5, and DA-2 samples. Testing was conducted on all composition variations with a temperature of 298K and a CO_2 pressure of ±2.5 bar which was later converted into atm. The duration of the test was determined from the saturation conditions on the PAN sample. The PAN sample experienced saturation at 185 minutes. However, to ensure that the sample was in equilibrium, testing was carried out until the 200th minute and the equilibrium CO_2 pressure value was obtained at that minute. Thus, the CO_2 adsorption test was carried out on all samples for 200 minutes.

Table 3. CO_2 Adsorption Results for PAN, DA – 2, and AFM – 5

Sample (wt%)	Pi (atm)	Pt (atm)	t (minute)	CO_2 mass (g)	Qe (mmol/g)	Qe (mg/g)	Sample Code
PAN/ZrO_2/$CsPbBr_3$ (100 : 0 : 0)	2.49711	2.310	200	1.343	7.22	63.42	PAN
PAN/ZrO_2/$CsPbBr_3$ (16.67 : 0 : 83.33)	2.5267	1.905	200	1.343	31.42	276.08	DA - 2
PAN/ZrO_2/$CsPbBr_3$ (11.75 : 0.15 : 88.10)	2.52672	1.905	200	0	42.89	376.82	AFM-5

Table 3 presents various adsorption parameters. "Pi" refers to the initial pressure of CO_2 gas injected into the adsorption apparatus. "Pt" denotes the final pressure when the sample reaches equilibrium or saturation. "t" indicates the time required for the sample to reach saturation or equilibrium. "CO_2 mass" represents the estimated amount of CO_2 gas adsorbed by the nanofiber. "Qe" denotes the amount of CO_2 adsorbed at equilibrium per unit mass of the PAN/ZrO_2/$CsPbBr_3$ nanofiber.

Based on Table 3, each variation exhibits different CO_2 adsorption capacities. This can be observed from the performance of each sample. The pure PAN sample exhibited the lowest adsorption capacity at 63.42 mg/g. The DA–2 sample showed a higher adsorption capacity than pure PAN, with a value of 276.08 mg/g. The AFM–5 sample demonstrated the highest CO_2 adsorption capacity, reaching 376.82 mg/g. However, despite their adsorption capacities, both PAN and DA–2 samples successfully adsorbed a total of 1.343 grams of CO_2, while the AFM–5 variation showed no measurable CO_2 uptake.

This phenomenon has been discussed in several scientific articles. For example, (Kretzschmar et al., 2021) reported that CO_2 adsorption on carbonized polyacrylonitrile (PAN)-based nanofibers occurs very slowly and results in relatively low adsorption capacity, especially at intermediate pressures such as 2.5 bar. Their study explained that for structures with ultramicropores (0.5–2 nm), the CO_2 adsorption capacity typically ranges between 0.1 to 1 mmol/g. Another possible explanation is the desorption of CO_2 when the system is opened before weighing. Additionally, the type of interaction between CO_2 molecules and the adsorbent surface—whether physical or chemical—greatly influences the stability of the adsorbed CO_2 molecules.A similar issue was also discussed by (Satar et al., 2019), who stated that in small-scale systems with metal chambers, a decrease in CO_2 pressure does not necessarily indicate adsorption by the nanofiber material. Instead, it may result from temporary physical interactions between CO_2 molecules and the metal surface of the chamber. CO_2 may be temporarily adsorbed on the metal surface via weak physical forces and then released upon pressure change, without contributing to the mass change of the primary adsorbent.

The CO_2 adsorption experiment was conducted in a closed system at a pressure of 2.5 bar for 200 minutes. The results showed a consistent decrease in gas pressure without any indication of leakage. However, no mass change was observed in the nanofibers before and after the test, even though equilibrium had been reached. This may be attributed to the very small amount of CO_2 adsorbed, the predominance of physical adsorption, or desorption occurring upon system depressurization. Furthermore, the possibility of temporary CO_2 adsorption on the metal chamber walls may also have contributed to the result, without increasing the mass of the nanofiber adsorbent.

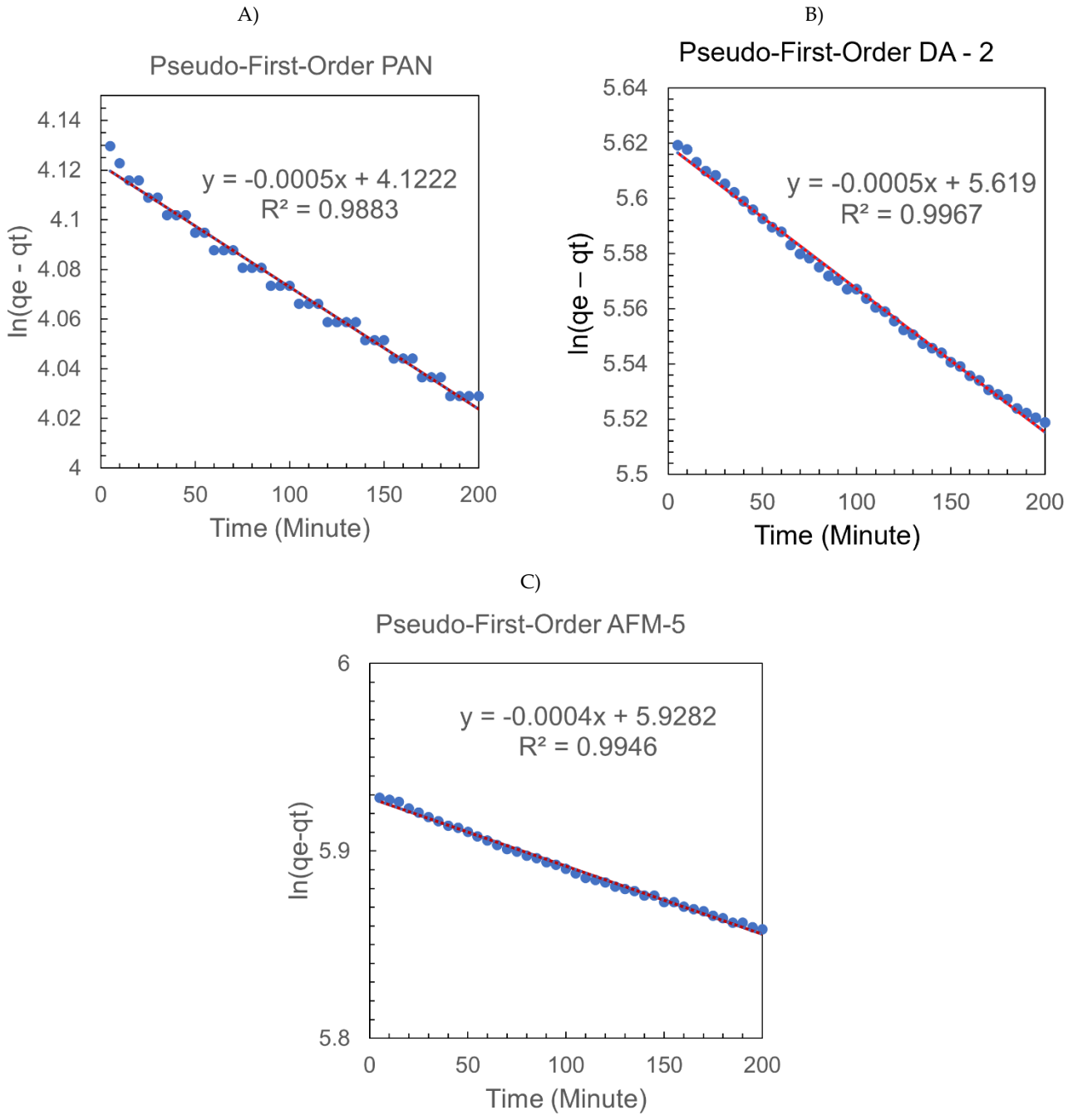

Fig 8. *Pseudo – First – Order* Kinetic Model of PAN, DA – 2, and AFM – 5

In this study, three CO_2 adsorption kinetic models were used, namely, *Pseudo-First-Order*, *Pseudo-Second-Order*, and *Intra-particle Diffusion*. The kinetic model for *Pseudo-First-Order* indicates that an adsorbent has a physical CO_2 adsorption mechanism (physisorption), while *Pseudo-Second-Order* indicates that an adsorbent has a chemical CO_2 adsorption mechanism (chemisorption) (Zang et al., 2024). The *Intraparticle Diffusion* kinetic model was used to validate the impact of mass transfer resistance on the interaction of CO_2 with the PAN/ZrO_2/$CsPbBr_3$ composite (Abdelmegeed et al., 2024). When using the intraparticle diffusion adsorption kinetic model, the process involves three steps: intraparticle diffusion, external diffusion or boundary layer diffusion, and the final equilibrium stage. In this kinetic model, if the intercept value (C) equals zero ($C = 0$), it indicates that intraparticle diffusion is the sole rate-limiting step in the adsorption process. However, a non-zero intercept value ($C \neq 0$) suggests a contribution from boundary layer diffusion. This implies that the adsorption rate is not solely governed by the pure diffusion of molecules into the pores of the adsorbent, but is also influenced by resistance at the outer surface of the particle. Therefore, when

C ≠ 0, the CO_2 adsorption mechanism on the nanofiber is most likely controlled by a combination of intraparticle diffusion and surface film diffusion, or by dominant instantaneous surface adsorption at the initial stage, which may result from uneven CO_2 flow or surface structures that hinder molecular transfer (Kristianto et al., 2022; Teng et al., 2017).

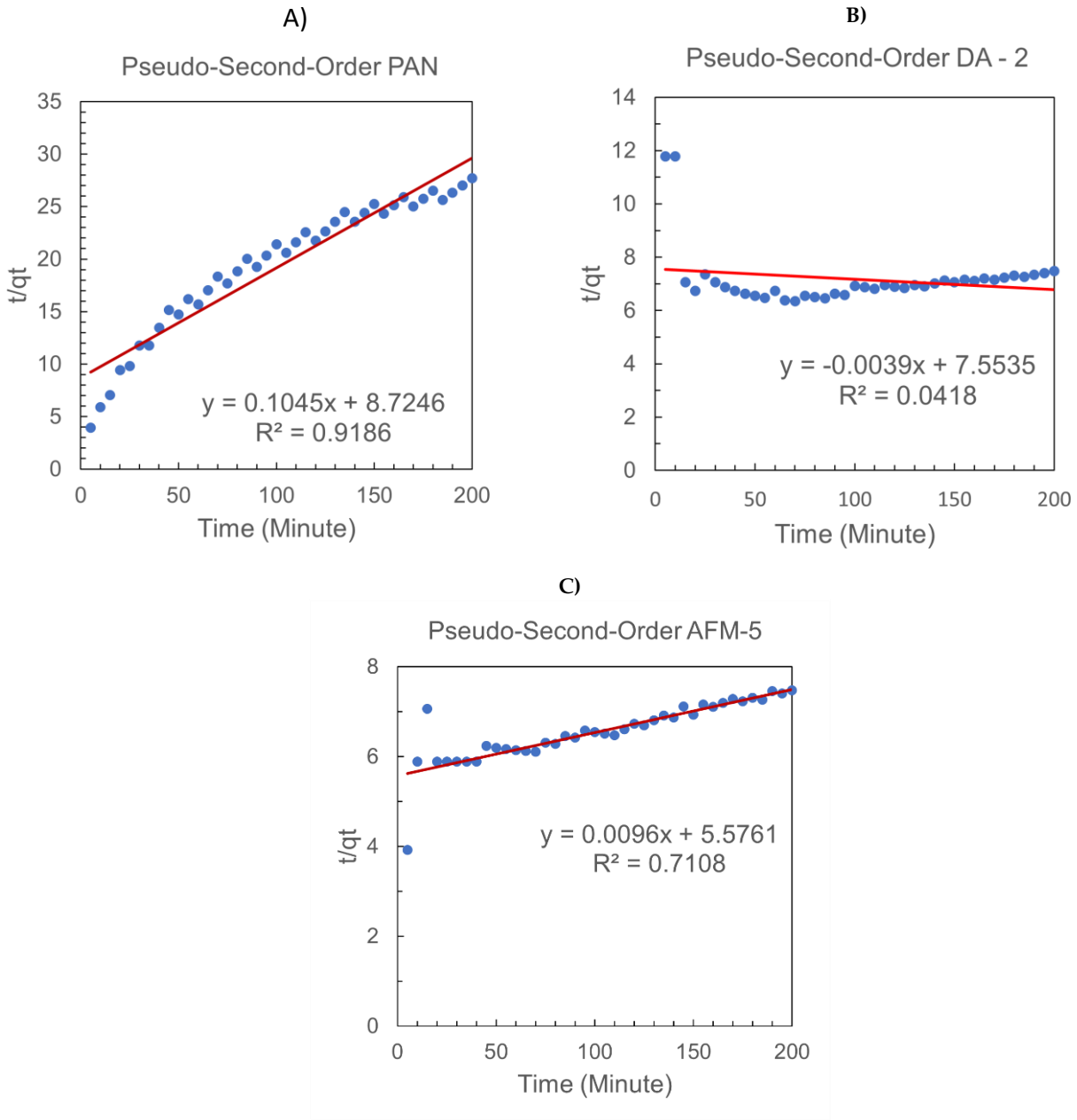

Fig 9. *Pseudo – First – Order* Kinetic Model of PAN, DA – 2, and AFM – 5

As seen in Table 4., Table 5., and Table 6., "Kf" represents the adsorption rate constant for the Pseudo-First-Order (PFO) kinetic model. "H" denotes the adsorption rate constant for the Pseudo-Second-Order (PSO) model. "Kid" is the adsorption rate constant for the intraparticle diffusion model. "C" is the intercept associated with the boundary layer thickness. "Qe" indicates the adsorption capacity at equilibrium conditions (Gunawan et al., 2018). To understand how CO_2 adsorption occurs on the fabricated nanofiber materials, two kinetic models were applied: the Pseudo-First-Order (PFO) and Pseudo-Second-Order (PSO) models. These models are used to estimate the adsorption rate and capacity of CO_2 for each sample, as well as to identify the dominant adsorption mechanism—whether physical or chemical.

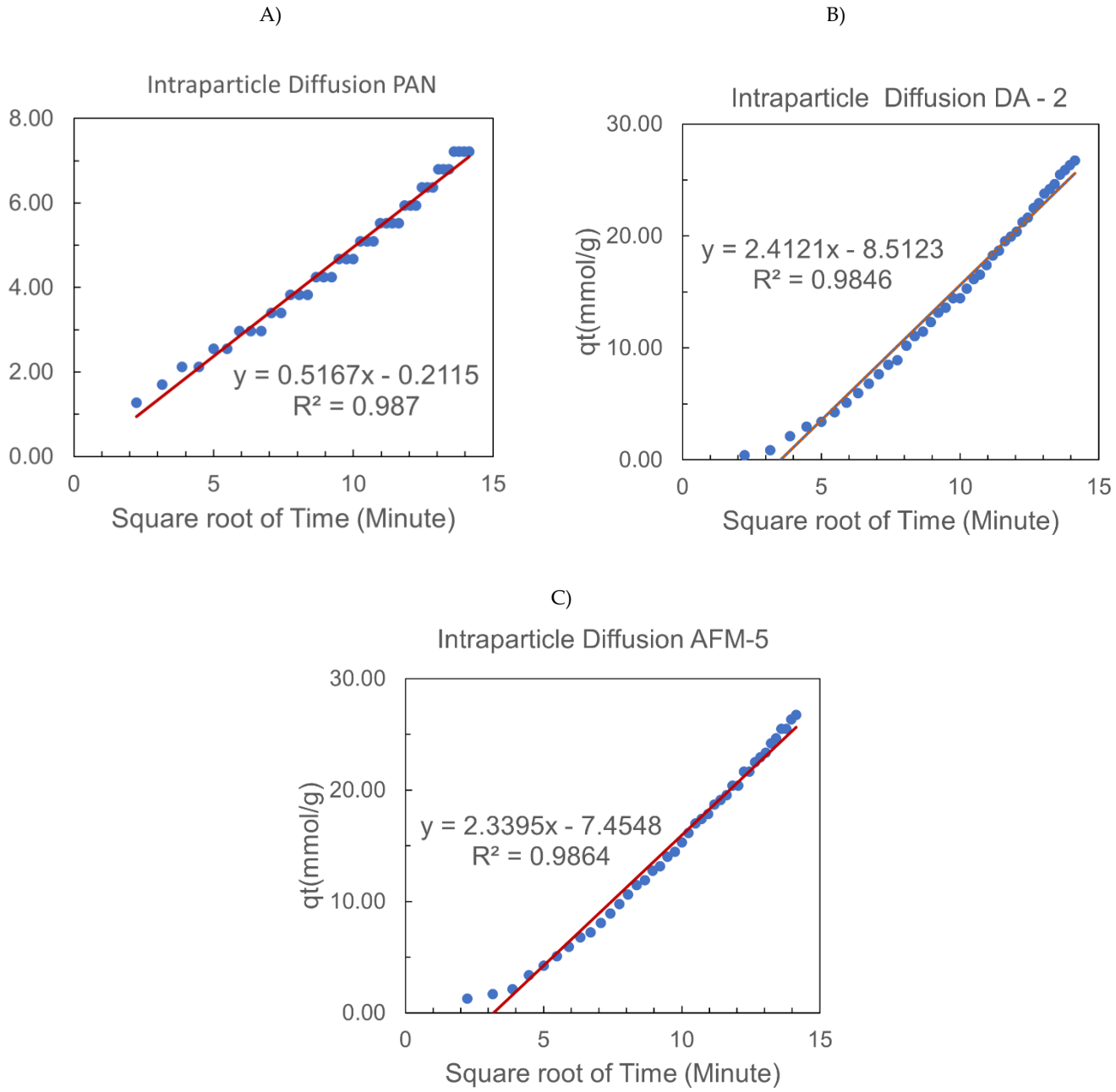

Fig 10. *Intraparticle Diffusion* Kinetic Model of PAN, DA – 2, and AFM – 5

In the PAN sample, the Pseudo-First-Order (PFO) model showed a fairly good fit, with an equilibrium adsorption capacity (Qe) of 4.1222 mmol/g and an R^2 value of 0.9883. This indicates that the PFO model adequately describes the adsorption process occurring in PAN. Meanwhile, the Pseudo-Second-Order (PSO) model yielded a Qe value of 8.7246 mmol/g, which is significantly higher than that obtained from the PFO model, even though its R^2 value was only 0.9186, slightly lower than that of PFO. The large discrepancy in the Qe values suggests that the PSO model is unrealistic and likely not suitable for describing the adsorption behavior of pure PAN. Therefore, it can be concluded that the dominant mechanism of CO_2 adsorption on PAN is physical rather than chemical bonding. In the DA – 2 sample, which consists of nanofibers modified with $CsPbBr_3$, the Pseudo-First-Order (PFO) model again demonstrated a very good fit, with a Qe value of 5.619 mmol/g and an R^2 value of 0.9967, indicating an almost perfect correlation. In contrast, the Pseudo-Second-Order (PSO) model yielded an R^2 value of only 0.0418, suggesting that this model is not suitable for describing the adsorption process in this sample. Although the Qe value predicted by the PSO model was relatively high at 7.5535 mmol/g, it is considered inaccurate due to the low R^2 value. These results indicate that the addition of $CsPbBr_3$ does enhance the adsorption capacity, but it does not change the type of adsorption mechanism, which remains predominantly physical

in nature. A similar result was observed in the AFM – 5 sample, which had been modified with the addition of $CsPbBr_3$ and ZrO_2. The Pseudo-First-Order (PFO) model once again provided the best fit, with a Qe value of 5.9282 mmol/g and an R^2 value of 0.9946, indicating an almost perfect agreement between the experimental data and the model. In contrast, the Pseudo-Second-Order (PSO) model resulted in a low R^2 value of only 0.7108, which is insufficient for reliable interpretation. Therefore, it does not alter the adsorption mechanism of the material. This suggests that the adsorption process still occurs through physical interaction rather than chemical bonding.

Table 4. Pseudo-First-Order Kinetics of $PAN/ZrO_2/CsPbBr_3$ Nanofibers

Sample **(wt%)**	**Pseudo First Order (PFO)**			Sample Code
	K_f	**Q_e (mg/g)**	**R^2**	
$PAN/ZrO_2/CsPbBr_3$ (100 : 0 : 0)	0.0005	4.1222	0.9883	PAN
$PAN/ZrO_2/CsPbBr_3$ (16.67 : 0 : 83.33)	0.0005	5.619	0.9967	DA – 2
$PAN/ZrO_2/CsPbBr_3$ (11.75 : 0.15 : 88.10)	0.0004	5.9282	0.9946	AFM – 5

Overall, the PFO model provides the most appropriate fit across all nanofiber variations. The adsorption capacity (Qe) calculated from this model consistently increases from PAN to AFM – 5, indicating that the incorporation of functional materials such as $CsPbBr_3$ and ZrO_2 effectively improves the nanofibers' ability to capture CO_2. However, the PSO model is unsuitable due to its low R^2 values and inaccurate Qe estimates. This implies that despite structural modifications, the primary mechanism for CO_2 adsorption remains weak physical interaction rather than strong chemical reactions.

Table 5. Pseudo-Second-Order Kinetics of $PAN/ZrO_2/CsPbBr_3$ Nanofibers

Sample (wt%)	**Pseudo Second Order (PSO)**			Sample Code
	H	**Q_e**	**R^2**	
$PAN/ZrO_2/CsPbBr_3$ (100 : 0 : 0)	0.1045	8.7246	0.9186	PAN
$PAN/ZrO_2/CsPbBr_3$ (16.67 : 0 : 83.33)	0.0039	7.5535	0.0418	DA – 2
$PAN/ZrO_2/CsPbBr_3$ (11.75 : 0.15 : 88.10)	0.0096	5.5761	0.7108	AFM – 5

To investigate the role of diffusion into the material's pores, the Weber–Morris intraparticle diffusion model was applied, as shown in Fig 10. and Table 6, The intraparticle diffusion rate constant (Kid) exhibited a significant increase in DA – 2 and AFM – 5, with respective values of 2.4121 and 2.3395 $mg/g{\cdot}min^{0.5}$, compared to PAN (0.5167 $mg/g{\cdot}min^{0.5}$). This indicates that the incorporation of $CsPbBr_3$ and ZrO_2 significantly enhances the diffusion rate of CO_2 into the porous structure of the nanofibers. According to Table 6, high R^2 values were obtained for all three nanofiber sample variations: 0.987 for PAN, 0.9846 for DA – 2, and 0.9864 for AFM–5. These R^2 values, which are close to 1, indicate that the Weber–Morris model fits the CO_2 adsorption kinetics data very well across all variations. This confirms that intraparticle diffusion plays a dominant role in the mass transfer of CO_2 into the pores of the adsorbent. However, all variations exhibited negative intercept (C) values: –0.2115 for AFM–1, and –8.5123 and –7.4548 for DA – 2 and AFM–5, respectively. Theoretically, the intercept value should be positive, as it represents the boundary layer thickness. A negative intercept suggests a possible initial delay before effective intraparticle diffusion occurs. This may be due to rapid adsorption on the external surface of the particles at the early stage or due to interphase diffusion imbalances (Obradovic, 2020). Nevertheless, the high Kid values still indicate that intraparticle diffusion plays a significant role in the overall adsorption mechanism.

Table 6. Intraparticle Diffusion Kinetics Of $PAN/ZrO_2/CsPbBr_3$

Sample (wt%)	**Intra-Particle Diffusion**			Sammple Code
	K_{id}	**C**	**R^2**	
$PAN/ZrO_2/CsPbBr_3$ (100 : 0 : 0)	0.5167	-0.2115	0.987	PAN
$PAN/ZrO_2/CsPbBr_3$ (16.67 : 0 : 83.33)	2.4121	-8.5123	0.9846	DA – 2
$PAN/ZrO_2/CsPbBr_3$ (11.75 : 0.15 : 88.10)	2.3395	-7.4548	0.9864	AFM – 5

Overall, the results from the three models indicate that the PFO model is the most appropriate for describing the CO_2 adsorption kinetics in the PAN/ZrO_2/$CsPbBr_3$ nanofiber system. The adsorption mechanism is predominantly physical, supported by diffusion into the material's pores, while the contribution of chemical interaction appears to be minimal.

4. Conclusion

This study successfully developed PAN/$CsPbBr_3$/ZrO_2 composite nanofibers through electrospinning and demonstrated their potential as CO_2 adsorbents. The incorporation of $CsPbBr_3$ significantly increased the adsorption capacity, while the addition of ZrO_2 enhanced nanofiber uniformity, reduced bead formation, and improved structural stability. Kinetic modeling revealed that the Pseudo-First-Order (PFO) model best described the adsorption behavior across all samples, indicating a dominant physical adsorption mechanism. Intraparticle diffusion analysis further confirmed the role of porous structure in facilitating CO_2 mass transfer, especially in AFM–5. Despite the presence of chemical components, chemisorption played a minimal role. Overall, AFM–5 exhibited the highest CO_2 adsorption performance and optimal kinetic characteristics, proving that the synergistic effect of $CsPbBr_3$ and ZrO_2 in a PAN matrix can effectively enhance CO_2 capture efficiency.

Acknowledgment. The authors would like to express their sincere gratitude to the Laboratory of Materials and Metallurgical Engineering, Institut Teknologi Sepuluh Nopember (ITS), for providing the necessary facilities, equipment, and support throughout the research. The resources and assistance made available by the laboratory played a crucial role in ensuring the smooth execution of this study and the achievement of meaningful results.

Declaration of Generative AI and AI-assisted technologies in the writing process. During the preparation of this work, the author(s) used Chat GPT-3.0 to improve readability and language understanding. After utilizing this AI technology, the author(s) meticulously reviewed and amended the content as required, ensuring its accuracy and completeness. The author(s) assume(s) complete accountability for the content of the publication.

Conflict-of-Interest Statement. The authors declare that they have no conflict of interest.

Funding. This research did not receive any specific grant from funding agencies in the public, commercial, or not-for-profit sectors.

References

Abdelmegeed, A.F., Sayed, M., Abbas, M., Abdel Moniem, S.M., Farag, R.S., Sayed, A.Z., Naga, S.M., 2024. Hydroxyapatite-magnetite nanocomposites: Synthesis and superior adsorption properties for lead ion removal, with insights into intraparticle diffusion, kinetic modeling, and phase dependency. Ceramics International 50, 36074–36087.

Ahmadi Bonakdar, M., Rodrigue, D., 2024. Electrospinning: Processes, Structures, and Materials. Macromol 4, 58–103.

Akhil, S., Dutt, V.G.V., Mishra, N., 2021. Surface modification for improving the photoredox activity of $CsPbBr_3$ nanocrystals. Nanoscale Adv. 3, 2547–2553.

Avossa, J., Herwig, G., Toncelli, C., Itel, F., Rossi, R.M., 2022. Electrospinning based on benign solvents: current definitions, implications and strategies. Green Chem. 24, 2347–2375.

Bakar, S.S.S., Fong, K.C., Eleyas, A., Nazeri, M.F.M., 2018. Effect of Voltage and Flow Rate Electrospinning Parameters on Polyacrylonitrile Electrospun Fibers. IOP Conf. Ser.: Mater. Sci. Eng. 318, 012076.

Barua, B., Saha, M.C., 2018. Influence of humidity, temperature, and annealing on microstructure and tensile properties of electrospun polyacrylonitrile nanofibers. Polymer Engineering & Sci 58, 998–1009.

Beknalkar, S.A., Teli, A.M., Harale, N.S., Patil, D.S., Pawar, S.A., Shin, J.C., Patil, P.S., 2021. Fabrication of high energy density supercapacitor device based on hollow iridium oxide nanofibers by single nozzle electrospinning. Applied Surface Science 546, 149102.

Beltzung, A., Klaue, A., Colombo, C., Wu, H., Storti, G., Morbidelli, M., 2018. Polyacrylonitrile Nanoparticle-Derived Hierarchical Structure for CO_2 Capture. Energy Tech 6, 718–727.

Bonakdar, M.A., Hamdi, O., Nazarenko, Y., Ariya, P.A., Rodrigue, D., 2023. Highly porous biobased membranes via electrospinning of PBS and CTAB. Polymer 280, 126045.

Chen, Haitao, Li, R., Guo, A., Xia, Y., 2021. Highly fluorescent CsPbBr3/TiO2 core/shell perovskite nanocrystals with excellent stability. SN Appl. Sci. 3, 654.

Chen, Hongyu, Wang, Y., Wang, J., Liu, W., 2021. Thermal Stability of CsPbBr3 Perovskite Quantum Dots Assembled with SBA-15. Coatings 11, 953.

Darmayanti, M.G., Tuck, K.L., Thang, S.H., 2024. Carbon Dioxide Capture by Emerging Innovative Polymers: Status and Perspectives. Advanced Materials 36, 2403324.

Fajariah, A.R., Aprilia, A., Adiperdana, B., Faizal, F., Safriani, L., 2023. Effect of Applied Voltage to the Electrospinning Process on the Structure and Morphology of Tio2 Nanofiber as Dssc Photoanode.

Gunawan, T., Wijiyanti, R., Widiastuti, N., 2018. Adsorption–desorption of CO_2 on zeolite-Y-templated carbon at various temperatures. RSC Adv. 8, 41594–41602.

Guo, X., Wang, L., Song, S., Liu, H., Zhang, Z., Wang, W., 2025. CsPbBr3 perovskite quantum dots with excellent water stability and optical properties synthetized through modifying with 6-aminohexanoic acid. Journal of Alloys and Compounds 1010, 177163.

Köck, E.-M., Kogler, M., Götsch, T., Schlicker, L., Bekheet, M.F., Doran, A., Gurlo, A., Klötzer, B., Petermüller, B., Schildhammer, D., Yigit, N., Penner, S., 2017. Surface chemistry of pure tetragonal ZrO_2 and gas-phase dependence of the tetragonal-to-monoclinic ZrO_2 transformation. Dalton Trans. 46, 4554–4570.

Kretzschmar, A., Selmert, V., Weinrich, H., Kungl, H., Tempel, H., Eichel, R., 2021. Study of CO_2 Sorption Kinetics on Electrospun Polyacrylonitrile-Based Carbon Nanofibers. Chem Eng & Technol 44, 1168–1177.

Kristianto, H., Manurung, N., Wardhani, I.K., Prasetyo, S., Sugih, A.K., Arbita, A.A., 2022. A kinetic, isotherm adsorption, and thermodynamic study of Congo red coagulation using *Leucaena* crude extract as natural coagulant. Water Practice and Technology 17, 1332–1346.

Kwon, T.-G., Jun Kim, B., Hyeon Jo, O., Kang, B.-G., Wook Kang, S., 2022. Synthesis of surface-tuned polyacrylonitrile particles and its application to CO2 separation. Journal of Industrial and Engineering Chemistry 109, 155–160.

Liu, Z., Ju, K., Wang, Z., Li, W., Ke, H., He, J., 2019. Electrospun Jets Number and Nanofiber Morphology Effected by Voltage Value: Numerical Simulation and Experimental Verification. Nanoscale Res Lett 14, 310.

Lusiola, T., Ichangi, A., Weil, D., Sebastian, T., Aneziris, C., Graule, T., Clemens, F., 2023. Electrospinning of ZrO2 fibers without sol-gel methods: Effect of inorganic Zr-source on electrospinning properties and phase composition. Open Ceramics 13, 100324.

Ma, C., Bai, J., Hu, X., Jiang, Z., Wang, L., 2023. Nitrogen-doped porous carbons from polyacrylonitrile fiber as effective CO2 adsorbents. Journal of Environmental Sciences 125, 533–543.

Mahmood, H.S., Jawad, M.K., 2019. Antibacterial activity of chitosan/PAN blend prepared at different ratios. Presented at the Technologies And Materials For Renewable Energy, Environment And Sustainability: TMREES19Gr, Athens, Greece, p. 020078.

Moore, J.K., Marti, R.M., Guiver, M.D., Du, N., Conradi, M.S., Hayes, S.E., 2018. CO_2 Adsorption on PIMs Studied with ^{13}C NMR Spectroscopy. J. Phys. Chem. C 122, 4403–4408.

Obradovic, B., 2020. Guidelines for general adsorption kinetics modeling. Hem Ind 74, 65–70.

Patel, H.A., Byun, J., Yavuz, C.T., 2017. Carbon Dioxide Capture Adsorbents: Chemistry and Methods. ChemSusChem 10, 1303–

Quan, C., Zhou, Y., Wang, J., Wu, C., Gao, N., 2023. Biomass-based carbon materials for CO2 capture: A review. Journal of CO2 Utilization 68, 102373.

Satar, E., Nyfeler, P., Bereiter, B., Pascale, C., Niederhauser, B., Leuenberger, M., 2019. Investigation of adsorption/desorption behavior of small volumecylinders and its relevance for atmospheric trace gas analysis.

Shah, C., Raut, S., Kacha, H., Patel, H., Shah, M., 2021. Carbon capture using membrane-based materials and its utilization pathways. Chem. Pap. 75, 4413–4429.

Shaki, H., 2023. The use of electrospun nanofibers for absorption and separation of carbon dioxide: A review. Journal of Industrial Textiles 53, 15280837231160290.

Shi, Y., Su, X., Wang, X., Ding, M., 2024. In Situ Synthesis of CsPbX3/Polyacrylonitrile Nanofibers with Water-Stability and Color-Tunability for Anti-Counterfeiting and LEDs. Polymers 16, 1568.

Song, X., Ding, Y., Zhang, J., Jiang, C., Liu, Z., Lin, C., Zheng, W., Zeng, Y., 2023. Thermophysical and mechanical properties of cubic, tetragonal and monoclinic ZrO2. Journal of Materials Research and Technology 23, 648–655.

Teng, Y., Liu, Z., Xu, G., Zhang, K., 2017. Desorption Kinetics and Mechanisms of CO2 on Amine-Based Mesoporous Silica Materials. Energies 10, 115.

Tourzani, A.A., Hormozi, F., Asadollahzadeh, M., Torkaman, R., 2023. Effective CO2 capture by using poly (acrylonitrile) nanofibers based on the radiation grafting procedure in fixed-bed adsorption column. Sci Rep 13, 6173.

Wang, Q., Xie, J., Huang, H., Ni, W., Xue, Q., 2024. Enhanced ambient-stability and charge transport property of the CsPbBr3@Polyaniline. Journal of Luminescence 275, 120770.

Zaker, A., Ben Hammouda, S., Sun, J., Wang, X., Li, X., Chen, Z., 2023. Carbon-based materials for CO2 capture: Their production, modification and performance. Journal of Environmental Chemical Engineering 11, 109741.

Zang, P., Tang, J., Zhang, H., Wang, X., Zhao, Peiyu, Cui, L., Chen, J., Zhao, Pei, Dong, Y., 2024. Insights into amine-resin matching strategy for CO2 capture: Adsorption performance tests and Mechanistic investigation. Separation and Purification Technology 331, 125622.

Zhou, Y., Liu, L., Li, G., Hu, C., 2021. Insights into the Influence of ZrO_2 Crystal Structures on Methyl Laurate Hydrogenation over Co/ZrO_2 Catalysts. ACS Catal. 11, 7099–7113.